Phys. Lett. B 850 (2024) 138550

Contents lists available at ScienceDirect

Physics Letters B

journal homepage: www.elsevier.com/locate/physletb

Letter

Constraining the pΛ interaction from a combined analysis of scattering data and correlation functions

D.L. Mihaylov [a,b,*], J. Haidenbauer [c], V. Mantovani Sarti [a]

[a] Technische Universität München, Physics Department, James-Franck-Str., Garching, 85748, Germany
[b] Sofia University, Faculty of Physics, 5 J. Bourchier Blvd, Sofia, 1164, Bulgaria
[c] Forschungszentrum Jülich, Institute for Advanced Simulation (IAS-4), Jülich, 52428, Germany

ARTICLE INFO

Editor: A. Schwenk

Keywords:
Scattering
Femtoscopy
Chiral effective field theory

ABSTRACT

This work provides the first combined analysis of low-energy pΛ scattering, considering both cross section and correlation data. The obtained results establish the most stringent constraints to date on the two-body pΛ interaction, pointing to a weaker attraction than so far accepted. The best set of scattering lengths for the spin singlet and triplet are found to range from $f_0, f_1 = (2.1, 1.56)$ to $(3.34, 1.18)$ fm. With a chiral NY potential fine-tuned to those scattering parameters, the in-medium properties of the Λ are explored and a potential depth of $U_\Lambda = -36.3 \pm 1.3(\text{stat})^{+2.5}_{-6.2}(\text{syst})$ MeV is found at nuclear matter saturation density.

1. Introduction

The strong interaction between nucleons (N) and hyperons (Y = Λ, Σ,Ξ) plays a significant role in various aspects of nuclear and hadronic physics, ranging from the structure and properties of hypernuclei to the Equation of State (EoS) of neutron star (NS) matter [1,2]. The recent observations of gravitational waves emitted from NS mergers [3,4] and precise constraints on NS radii provided by the NICER collaboration [5–8] triggered a renewed interest in the presence of strange degrees of freedom in these compact objects [9,10].

Specifically, the NΛ system represents an important pillar for our understanding of the low-energy QCD dynamics between ordinary matter and strange particles [11]. Chiral effective field theory (χEFT) [12–15] is an excellent tool to study the NΛ interaction, since it offers the possibility to systematically improve the results by considering higher-order terms in the Lagrangian. These effective approaches rely on the availability of experimental data to determine the a priori unknown low-energy constants (LECs) associated with the contact interactions included in the Lagrangian. Until recently, the experimental constraints on the NΛ interaction, and, in general, on the strangeness $S = -1$ baryon-baryon interaction, consisted primarily of scattering data [16–18] and measurements of Λ-hypernuclei binding energies [1,19]. Elastic and inelastic cross section data, probing the transition NΛ ↔ NΣ, are relatively scarce and not available down to the threshold. Results from the COSY experiment delivered input on the NΛ − NΣ dynamics by studying the $pp \to pK^+\Lambda$ reaction [20,21]. New scattering measurements on both NΛ and NΣ were reported by the CLAS [22] and E40 [23–25] collaborations, adding constraints at higher momenta. Additionally, measured binding energies and lifetimes of light Λ-hypernuclei [1] provide complementary information on the strength of the NΛ interaction, for example with regard to the hypertriton [26,27] specifically on the singlet state [14].

Data on hypernuclei in the medium and heavy mass regime have been employed to deduce the depth of the Λ single-particle potential U_Λ in infinite nuclear matter at nuclear saturation density $\rho_0 = 0.166$ fm^{-1}. An overall attraction of $-27 \sim -30$ MeV is typically reported [1,28–30], and this benchmark eventually serves as input for studies aiming to infer the behavior of Λ hyperons at NS core densities, reaching few times ρ_0. Specifically, in microscopic investigations that commence with NY potentials describing NΛ and NΣ scattering data, the generally somewhat too attractive contribution from the two-body interaction is counterbalanced by an appropriate repulsive three-body NNΛ component to meet the ≈ -30 MeV constraint [31,32]. The interplay between two- and three-body contributions is also considered in a recent phenomenological analysis of Λ-hypernuclei [30].

In the last years, novel data based on two-particle correlations, involving strange hadrons, have become available and offer high-precision experimental insight into the $S = -1, -2, -3$ baryon-baryon interaction [33–39]. The recent measurement of the pΛ correlation function in pp collisions at $\sqrt{s} = 13$ TeV by the ALICE Collabora-

* Corresponding author.
E-mail addresses: dimitar.mihaylov@mytum.de (D.L. Mihaylov), j.haidenbauer@fz-juelich.de (J. Haidenbauer), valentina.mantovani-sarti@tum.de (V. Mantovani Sarti).

https://doi.org/10.1016/j.physletb.2024.138550
Received 13 February 2024; Received in revised form 26 February 2024; Accepted 26 February 2024
Available online 29 February 2024

tion [34] provided the most precise data on this system down to threshold, accompanied by the first experimental observation of the opening of the NΣ channel in a two-body final state. Ongoing and future experimental efforts are posed to advance our understanding of the NΛ interaction and the NΛ ↔ NΣ dynamics. These efforts include the utilization of polarized Λ beams and high-precision hypernuclear spectroscopy [40], as well as statistically improved correlation functions during the ongoing LHC Run 3 data taking [41].

In this work, we, for the first time, perform a combined analysis of available NΛ scattering and correlation data to constrain the corresponding pΛ scattering parameters. The present study utilizes an Usmani-type potential and an interaction based on χEFT. Anticipating our main finding, the analysis suggests an overall less attractive NΛ interaction compared to what has formed the basis for theoretical investigations so far. To explore the possible implications for the NS scenarios [31,32], appropriately re-adjusted chiral potentials are employed to evaluate the single-particle potential U_Λ at ρ_0.

2. pΛ interaction

For the analysis of the pΛ correlation data at low momenta, we employ wave functions generated from two different types of potentials. To thoroughly explore the sensitivity of the effective range parameters to the measured pΛ correlation functions, we use the Usmani potential [42], which includes spin dependence but lacks coupling to the NΣ channel. This allows for a realistic description of the NΛ interaction below the NΣ threshold, which is relevant for determining the effective range parameters. We use the expression for the potential given in Ref. [43]:

$$V_{\mathrm{p}\Lambda}(r) = V_C(r) - \left(\bar{V} - \frac{1}{4}V_\sigma \boldsymbol{\sigma}_\Lambda \cdot \boldsymbol{\sigma}_p\right) T_\pi^2(r). \tag{1}$$

The short range part of the interaction is dominated by a Woods-Saxon-type repulsive core V_C, while the long-range part of the interaction is modeled by a two-pion exchange tail constructed from a modified one-pion exchange tensor potential [43],

$$T_\pi(r) = \left(1 + \frac{3}{x} + \frac{3}{x^2}\right)\frac{e^{-x}}{x}\left(1 - e^{-cr^2}\right)^2, \tag{2}$$

where $x = m_\pi r \approx 0.7\,r$. We take over the parameters from [43], i.e. we use $c = 2$ fm^{-2} together with $\bar{V} = 6.2$ MeV and $V_\sigma = 0.25$ MeV, for the spin-independent part of the attractive potential and the spin-dependent part respectively. The expression for the repulsive core is

$$V_C(r) = W_C\left[1 + \exp\left(\frac{r - R_C}{d_C}\right)\right]^{-1}. \tag{3}$$

Its parameters (W_C, R_C, d_C) are phenomenological in nature, and thus, we will adjust them in accordance with the analyzed data. Specifically, we will vary them independently for the two NΛ spin states when exploring the spin dependence in detail, see below.

In addition, we employ a modern NY potential derived within SU(3) χEFT [13,14], specifically, we utilize the NY potential NLO19 established in Ref. [14]. This potential incorporates contributions up to next-to-leading order (NLO) in the chiral expansion, in particular it includes contributions from one- and two-pseudoscalar-meson exchange diagrams, involving the Goldstone bosons π, K, η, and from four-baryon contact terms (without and with two derivatives), where the latter encode the unresolved short-distance dynamics. The LECs associated with these contact terms are free parameters and have been established by a global fit to a set of 36 pΛ and NΣ low energy scattering data points [14], available since the 1960s. SU(3) flavor symmetry has been imposed which reduces the number of independent contact terms or LECs, respectively. Then, in the two S-wave states $^1S_0$ and $^3S_0$, which dominate the scattering observables at low energies, there are 10 LECs [14], with two of them inferred from the NN sector via the imposed SU(3) symmetry.

The present work incorporates the pΛ correlation data measured by ALICE as an additional experimental constraint [44]. To accommodate this, some of the LECs have to be varied in the search for the optimal strength of the NΛ interaction. Thereby, we aim at preserving the good description of the pΣ^+ and pΣ^- data, as well as the p$\Sigma^-\to$ nΛ transition cross section provided by the original potential [14]. The simplest and most efficient way to guarantee this is to relax the strict SU(3) symmetry for the contact interactions in the NΛ and NΣ forces [13,14]. Therefore, following the procedure in [45], we introduce an SU(3) symmetry breaking in the leading-order contact terms that contribute to the NΛ interaction in the relevant $^1S_0$ and $^3S_1$ partial waves. We emphasize that such an SU(3) symmetry breaking at NLO is well in line with χEFT and the associated power counting [13,46].

3. Analysis

The combined analysis of scattering and femtoscopic data is based on 12 data points for the pΛ elastic cross section, as well as six pΛ correlation functions measured in different ranges of pair transverse mass m_{T} in pp collisions at 13 TeV. In particular, six points of the cross section stem from the work of Alexander et al. [17], where we opt for those from the second choice of binning described in the corresponding work, while the remaining six data points are taken from the work of Sechi-Zorn et al. [16]. The femtoscopy data originates from the ALICE measurement of the pΛ correlation function in high-multiplicity (HM) pp collisions at 13 TeV [44]. When analyzed below the NΣ threshold, the S-waves are sufficient to account for the interaction. The parameters of the repulsive core $V_C(r)$ in Eq. (3) are fitted independently for the spin singlet (S = 0) and triplet (S = 1) states, resulting in a total of 6 free parameters. The Usmani potential has been integrated into the CATS framework [47], which is capable of evaluating the corresponding cross section and correlation function by solving the Schrödinger equation. While this is sufficient to describe the cross section data, femtoscopic data necessitates additional knowledge of the two-particle emission source $S(m_{\mathrm{T}}, r)$, as demanded by the Koonin-Pratt equation [48]

$$C(k) = \int S(m_{\mathrm{T}}, r)\left|\Psi(\vec{k}, \vec{r})\right|^2 d^3r. \tag{4}$$

Here, $C(k)$ represents the correlation as a function of the single-particle momentum k in the pair rest frame, while $\Psi(\vec{k}, \vec{r})$ is the wave function of the relative motion of the pair. The source $S(m_{\mathrm{T}}, r)$ is provided as a function of the relative distance between the particles r at the moment of their effective emission. The modeling of the source in small collision systems at the LHC has been extensively studied in several recent works [44,49,50], which provide compatible results on the source properties. In the present analysis, we adopt the CECA model [49], which operates based on a common emission source for all primordial particles. It accounts for particle production through the decay of short-lived resonances and incorporates an intrinsic m_{T} scaling of the source size, as observed in the data. The CECA framework utilizes three fit parameters to describe an effective hadronization surface on which the primordial particles are emitted. These particles are all moving radially away from the collision point, with their momentum distributions based on experimental measurements. The simulated primordial particles include protons, Λ hyperons, or resonances that decay into one of these species via the strong force. After the decay of the resonances, all final state particles of interest are grouped into pΛ pairs. Those satisfying the low-momentum condition $k < 100$ MeV/c are used to construct a distribution in r and m_{T}, which, when normalized, corresponds to the source function $S(m_{\mathrm{T}}, r)$. The resulting source is non-Gaussian, however, an effective Gaussian parameterization yields very similar results for $C(k)$. The main benefit of using the CECA framework is its ability to simultaneously model the pp as well as the pΛ source to reproduce the experimentally observed decreasing source size as a function of m_{T}. Consequently, this allows to calibrate the pΛ source to the pp correlation, which has been measured differentially in m_{T} by ALICE [44,51],

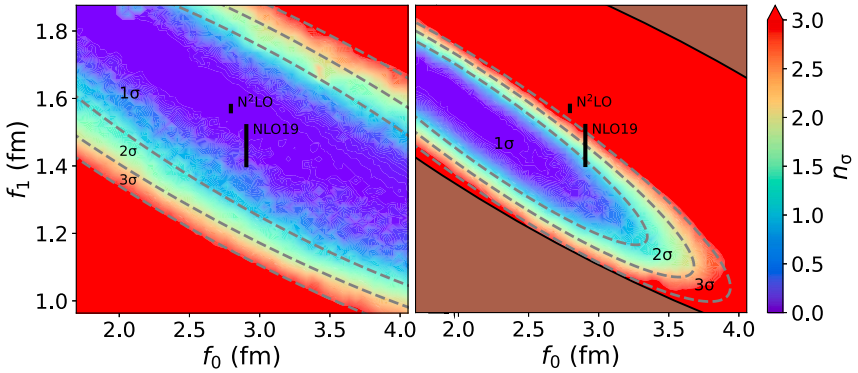

Fig. 1. Exclusion plots for the singlet (f_0) and triplet (f_1) pΛ scattering lengths based on the analysis of the cross section data (left panel) and on the combined analysis of cross section and correlation data (right panel). See text for details.

significantly improving the sensitivity of the correlation function to the interaction potential. In the present analysis, we perform a pre-fit of the pp correlations using the Argonne $v18$ potential [52], following the same procedure as described in [49]. However, out of the seven available m_T bins, we have omitted the last two due to issues with convergence at very low k. To eliminate any bias related to the assumption of a common source, the extracted source parameters from the pre-fit of the pp correlations are used as an initial guess for the pΛ system, after which they are re-fitted alongside the six interaction parameters, allowing a variation of 3 standard deviations (σ). Finally, we verify that the parameters converge to a proper local minimum. The remaining details on both the pp and pΛ fits, such as the inclusion of momentum resolution, feed-down, non-femtoscopic baseline, etc., are mirrored from the analysis of the same data described in [49].

The first objective of the present analysis is to quantify the allowed scattering lengths in the spin singlet/triplet channels (f_0, f_1), which can be accomplished by considering potentials of varying strengths in the CATS framework. Note that we use the sign convention where attractive/repulsive interactions are characterized by positive/negative scattering lengths. Both the cross section and the correlation function are composed of a weighted sum of the two channels, with respective weights of 1/4 and 3/4. The interactions in the two spin states are attractive and exhibit similar correlation shapes that differ in magnitude. Due to this similarity, the present analysis is not particularly sensitive to the individual scattering lengths of each spin channel, and a unique solution is not expected. Nevertheless, requiring that the two-body forces alone produce a bound hypertriton puts a lower limit on the strength of the interaction in the spin singlet channel. A concrete estimate is difficult to provide, however, judging from results for the hypertriton separation energy from Faddeev calculations employing modern YN potentials [14,15], values of $f_0 \lesssim 2.0$ fm are not realistic. Assuming that the hypertriton is solely bound by three-body forces is likewise unrealistic given the present estimates [53] and explicit calculations [54] of their possible contribution. In view of this the scan is performed for $f_0 > 1.6$ fm. The lack of a unique solution leads to convergence issues in the fit procedure. To address this problem, multiple fits are performed, each constrained within a specific small region of f_0 and f_1 values. The procedure is repeated until the entire desired parameter space is scanned. The best χ^2 of each individual step is saved, allowing the creation of an exclusion plot for f_0 and f_1. The estimator for the exclusion is the total $\chi^2 = \chi^2_{\text{scattering}} + \chi^2_{\text{femtoscopy}}$. The χ^2 is converted into a number of standard deviations (nσ) with respect to the best solution, accounting for a total of 9 degrees of freedom [55].

4. Results and discussion

The exclusion plot based on results with the Usmani potential is shown in Fig. 1. The axes correspond to the scattering lengths in the singlet f_0 and triplet f_1 channel, while the color code contains information on the compatibility with the data. The left panel is based on the analysis of only the cross section, while the right panel is the final result based on the combined analysis of femtoscopic and scattering data. The gray dashed lines mark the 1, 2 and 3σ exclusion regions. The black solid line, in the right panel, marks the border of a 3σ deviation with respect to the scattering data alone and is identical to the outer most dashed line from the left panel, while the shaded area depicts the region of even worse compatibility. As expected, there is a strong correlation between f_0 and f_1, and the inclusion of femtoscopy data into the analysis leads to a significant decrease in uncertainties. Values of $f_0 > 3.34$ fm or $f_1 < 1.18$ fm are disfavored by the data. The lower (upper) bound of f_0 (f_1) cannot be constrained within the investigated parameter space. Fig. 1 contains two vertical bars depicting the values of the scattering parameters based on the NLO19 [14] and the next-to-next-to-leading order N^{2}LO [15] potentials. The size of the markers represents the uncertainties related to the employed regulator (cutoff Λ) in the chiral NY potentials. Both of these values are located approximately in the middle of the phase space region allowed by the scattering data alone, which is not surprising, as the LECs of those potentials have, up to now, been fitted to that data. Nevertheless, the enhanced sensitivity of the combined analysis shows that the predicted scattering lengths are disfavored by as much as 4.8σ in the case of N^{2}LO. The NLO19 interaction is overall better in line with the present analysis, nevertheless, a systematic deviation of ca. 1-3 σ is observed, depending on the cutoff value. Indeed, the predictions by the potential with cutoff $\Lambda = 600$ MeV of $f_0 = 2.91$ fm and $f_1 = 1.41$ fm are in relatively good agreement, resulting in a deviation from the best solution of 1.1σ. On the other hand, a best fit of f_1, keeping $f_0 = 2.91$ fm fixed, yields $f_1 = 1.32 \pm 0.08$ fm. Clearly, due to the strong correlation between the two parameters, changing the value of f_0 will influence the outcome for f_1. For example, fixing $f_0 = 2.1$ fm implies the value $f_1 = 1.56 \pm 0.11$ fm. Considering the combined analysis (right panel in Fig. 1), the best set of solutions can be approximated by the relation

$$f_1 \approx 2.2 \text{ fm} - 0.3 f_0 \ (\pm 0.1 \text{ fm}) \tag{5}$$

for $f_0 \in (2.0, 2.9)$ fm. Table 1 in the Appendix provides multiple examples for scattering parameters and their compatibility to the data. These results indicate an overall less attractive interaction compared to the published chiral potentials.

As a next step we explore how this less attractive NΛ interaction affects predictions for the single-particle potential U_Λ at nuclear saturation density ρ_0 and its density dependence in general, considering the relevance of this quantity for the role of the Λ hyperon in neutron stars [9,10]. In Fig. 2, we present results for the single-particle potential $U_\Lambda(k_\Lambda = 0)$ as a function of the nuclear matter density ρ, evaluated self-consistently within a conventional G-matrix calculation. We employ the formalism described in detail in Refs. [31,56], where the so-called continuous choice is taken for the intermediate states, and the N^{3}LO

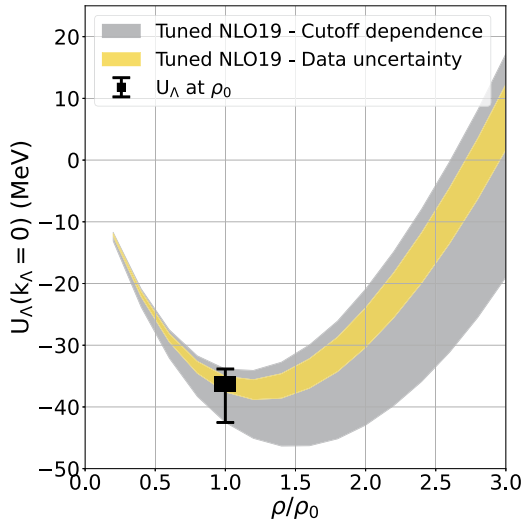

Fig. 2. Λ single-particle potential U_Λ as a function of the nuclear-matter density ρ with $\rho_0 = 0.166$ fm^{-3} being the nuclear-matter saturation density.

potential from [57] is used for the NN interaction. The NLO19(600) potential is chosen as a starting point from which, by readjusting some of its LECs to reproduce 8 combinations of the NΛ spin singlet and triplet scattering lengths within the 1σ region (points i to viii Table 1), we estimate the corresponding $U_\Lambda(\rho_0)$ given by the black square in Fig. 2. The vertical error bar represents the theoretical uncertainty estimated by considering the NLO19 potentials with different cutoffs (500 – 650 MeV), all re-fitted to describe the same set of scattering parameters. The final result is $U_\Lambda(\rho_0) = -36.3 \pm 1.3(\text{stat})^{+2.5}_{-6.2}(\text{syst})$ MeV, where the statistical uncertainty is associated with the data on the scattering parameters (right panel in Fig. 1) and the systematic with the cutoff dependence from the theory. The resulting theoretical uncertainty is large, as likewise reported in standard nuclear matter calculations with chiral nucleon-nucleon potentials [58,59]. Additionally, for the behavior of the potential depth as a function of ρ, we show in Fig. 2 the theoretical uncertainty (grey band) and the uncertainty from the combined data (yellow band). The predicted values for $U_\Lambda(\rho)$ are similar to the result for the original NLO19 potential. Our results at ρ_0 lie below the usually cited semi-empirical value of $U_\Lambda = -27 \sim -30$ MeV obtained from hypernuclei constraints [1,30]. This is in line with comparable G-matrix calculations where a similar overbinding feature has been observed when two-body-only contributions are taken into account, see, for example, [14,60]. In two recent works [31,32] an overall repulsion from a chiral NNY three-body force has been incorporated in the form of an effective density-dependent NY two-body potential [61]. This addition allows the authors to satisfy the ≈ −30 MeV hypernuclear constraint and, at the same time, suppresses the appearance of Λ hyperons for densities as realized in NS, i.e. offers a solution to the so-called "hyperon-puzzle" [2,9]. Our results are compatible with such a strategy. Quantitative constraints on this effective three-body force might become available in future correlation studies [62,63].

In conclusion, in this work we have presented the first combined analysis of low-energy femtoscopic and scattering data to constrain the S-wave scattering parameters of the pΛ interaction, resulting in the tightest limits available for future theoretical studies. The pΛ interaction is found to be overall less attractive than what has been indicated by the scattering data from the 1960s. We observe a strong, approximately linear (Eq. (5)), correlation between the values of the scattering lengths in the spin singlet and triplet states. The best solution, if f_0 is fixed to 2.1 fm, is $f_1 = 1.56 \pm 0.08$ fm. Lower f_0 values will eventually prohibit a hypertriton bound by two-body forces. The maximum (minimum) allowed values for f_0 (f_1) are 3.34 (1.18) fm.

Clearly, the accurate reproduction of low-energy NΛ data, like scattering cross sections and femtoscopic two-particle correlation functions, is an important requirement for realistic predictions of many-body systems. Thus, we have fine-tuned the chiral YN potential NLO19 to match the established scattering parameters in order to explore the impact on the in-medium properties of the Λ hyperon. The result with those NLO19 variants for $U_\Lambda(\rho_0)$ is ∼ −36 MeV, which implies an overbinding with regard to the nominal Λ binding energy in infinite nuclear matter. This is consistent with the current notion of an additional repulsion acting on the Λ within the medium, attributed to three-body forces. The presented results can serve as a state-of-the-art guideline for the contribution to be expected from two-body pΛ interactions.

Declaration of competing interest

The authors declare that they have no known competing financial interests or personal relationships that could have appeared to influence the work reported in this paper.

Data availability

In this work, we have only used previously measured and publicly available data, which can be accessed by following the references in the manuscript.

Acknowledgements

We would like to thank Prof. L. Fabbietti for her support and fruitful discussions which helped us in finalizing these results. This work was supported by the ORIGINS cluster DFG under Germany's Excellence Strategy - EXC2094 - 390783311 and the DFG through Grant SFB 1258 "Neutrinos and Dark Matter in Astro and Particle Physics". V.M.S. is supported by the Deutsche Forschungsgemeinschaft (DFG) through the grant MA 8660/1-1.

Appendix A

Table 1 provides details on the 8 different selected sets of $\{f_0,\ f_1\}$ values, chosen to represent the 1σ region of best compatibility to the combined data, as well as 3 points anchored to existing parameterizations of the chiral effective field theory [13–15]. The compatibility is estimated using the number of standard deviations, denoted as nσ, with respect to the best possible fit. We consider three scenarios: firstly, only the femtoscopy data is taken into account, resulting in nσ_{fmt}; secondly, only the scattering data is considered (nσ_{sct}); and thirdly, nσ_{tot} corresponds to the combined analysis presented in this work. It is essential to note that these three scenarios represent independent analyses, each having a different best solution as a baseline. Consequently, there is no straightforward relation between the three estimators.

Table 1
Summary table showing the compatibility of different scattering parameters to the femtocsopy data (nσ_{fmt}), scattering data (nσ_{sct}) as well as the combined analysis from the present work (nσ_{tot}). If the combined estimator nσ_{tot} is considered, solutions ii, v and vii represent a set of "best" solutions.

Usmani parameterization	f_0 (fm)	f_1 (fm)	nσ_{fmt}	nσ_{sct}	nσ_{tot}
NLO13(600)	2.91	1.54	5.2	0.0	4.6
NLO19(600)	2.91	1.41	1.7	0.4	1.1
N^{2}LO(550)	2.79	1.58	5.4	0.0	4.8
i	2.10	1.44	0.2	2.1	1.0
ii	**2.10**	**1.56**	**0.0**	**0.9**	**0.0**
iii	2.10	1.66	1.8	0.2	1.0
iv	2.50	1.32	0.2	2.2	1.1
v	**2.50**	**1.46**	**0.2**	**0.8**	**0.0**
vi	2.50	1.55	1.8	0.2	1.0
vii	**2.91**	**1.32**	**0.1**	**1.5**	**0.3**
viii	3.34	1.18	1.2	0.9	1.0

References

[1] A. Gal, E.V. Hungerford, D.J. Millener, Strangeness in nuclear physics, Rev. Mod. Phys. 88 (2016) 035004.
[2] L. Tolos, L. Fabbietti, Strangeness in nuclei and neutron stars, Prog. Part. Nucl. Phys. 112 (2020) 103770.
[3] B.P. Abbott, et al., LIGO Scientific, Virgo, GW170817: observation of gravitational waves from a binary neutron star inspiral, Phys. Rev. Lett. 119 (2017) 161101.
[4] B.P. Abbott, et al., LIGO Scientific, Virgo, Fermi GBM and others, Multi-messenger observations of a binary neutron star merger, Astrophys. J. Lett. 848 (2017) L12.
[5] M.C. Miller, et al., PSR J0030+0451 mass and radius from $NICER$ data and implications for the properties of neutron star matter, Astrophys. J. Lett. 887 (2019) L24.
[6] M.C. Miller, et al., The radius of PSR J0740+6620 from NICER and XMM-Newton data, Astrophys. J. Lett. 918 (2021) L28.
[7] T.E. Riley, et al., A $NICER$ view of PSR J0030+0451: millisecond pulsar parameter estimation, Astrophys. J. Lett. 887 (2019) L21.
[8] T.E. Riley, et al., A NICER view of the massive pulsar PSR J0740+6620 informed by radio timing and XMM-Newton spectroscopy, Astrophys. J. Lett. 918 (2021) L27.
[9] D. Chatterjee, I. Vidaña, Do hyperons exist in the interior of neutron stars?, Eur. Phys. J. A 52 (2016) 29.
[10] J. Schaffner-Bielich, Compact Star Physics, Cambridge University Press, 2020.
[11] B. Povh, Nuclear physics with hyperons, Prog. Part. Nucl. Phys. 5 (1981) 245–268.
[12] S. Weinberg, Nuclear forces from chiral Lagrangians, Phys. Lett. B 251 (1990) 288–292.
[13] J. Haidenbauer, S. Petschauer, N. Kaiser, U.-G. Meißner, A. Nogga, W. Weise, Hyperon-nucleon interaction at next-to-leading order in chiral effective field theory, Nucl. Phys. A 915 (2013) 24–58.
[14] J. Haidenbauer, U.-G. Meißner, A. Nogga, Hyperon–nucleon interaction within chiral effective field theory revisited, Eur. Phys. J. A 56 (2020) 91.
[15] J. Haidenbauer, U.-G. Meißner, A. Nogga, H. Le, Hyperon–nucleon interaction in chiral effective field theory at next-to-next-to-leading order, Eur. Phys. J. A 59 (2023) 63.
[16] B. Sechi-Zorn, B. Kehoe, J. Twitty, R.A. Burnstein, Low-energy Λ–proton elastic scattering, Phys. Rev. 175 (1968) 1735–1740.
[17] G. Alexander, U. Karshon, A. Shapira, G. Yekutieli, R. Engelmann, H. Filthuth, W. Lughofer, Study of the Λ–N system in low-energy Λ–p elastic scattering, Phys. Rev. 173 (1968) 1452–1460.
[18] F. Eisele, H. Filthuth, W. Foehlisch, V. Hepp, G. Zech, Elastic Σ^+–p scattering at low energies, Phys. Lett. B 37 (1971) 204–206.
[19] O. Hashimoto, H. Tamura, Spectroscopy of Lambda hypernuclei, Prog. Part. Nucl. Phys. 57 (2006) 564–653.
[20] M. Röder, et al., COSY-TOF, Final-state interactions in the process $\vec{p}p \to pK^+\Lambda$, Eur. Phys. J. A 49 (2013) 157.
[21] F. Hauenstein, et al., COSY-TOF, Determination of the spin triplet $p\Lambda$ scattering length from the final state interaction in the $\vec{p}p \to pK^+\Lambda$ reaction, Phys. Rev. C 95 (2017) 034001.
[22] J. Rowley, et al., CLAS, Improved Λp elastic scattering cross sections between 0.9 and 2.0 GeV/c and connections to the neutron star equation of state, Phys. Rev. Lett. 127 (2021) 272303.
[23] K. Miwa, et al., J-PARC E40, Precise measurement of differential cross sections of the $\Sigma^- p \to \Lambda n$ reaction in momentum range 470-650 MeV/c, Phys. Rev. Lett. 128 (2022) 072501.
[24] K. Miwa, et al., J-PARC E40, Measurement of the differential cross sections of the $\Sigma^- p$ elastic scattering in momentum range 470 to 850 MeV/c, Phys. Rev. C 104 (2021) 045204.
[25] T. Nanamura, et al., J-PARC E40, Measurement of differential cross sections for Σ+p elastic scattering in the momentum range 0.44–0.80 GeV/c, PTEP 2022 (2022) 093D01.
[26] S. Acharya, et al., ALICE, ${}^3_\Lambda$H and ${}^3_{\bar{\Lambda}}\overline{\text{H}}$ lifetime measurement in Pb-Pb collisions at $\sqrt{s_{\rm NN}} = 5.02$ TeV via two-body decay, Phys. Lett. B 797 (2019) 134905.
[27] J. Adam, et al., STAR, Measurement of the mass difference and the binding energy of the hypertriton and antihypertriton, Nat. Phys. 16 (2020) 409–412.
[28] D.J. Millener, C.B. Dover, A. Gal, Lambda nucleus single particle potentials, Phys. Rev. C 38 (1988) 2700–2708.
[29] E. Friedman, A. Gal, Constraints from Λ hypernuclei on the ΛNN content of the Λ-nucleus potential, Phys. Lett. B 837 (2023) 137669.
[30] E. Friedman, A. Gal, Λ hypernuclear potentials beyond linear density dependence, Nucl. Phys. A 1039 (2023) 122725.
[31] D. Gerstung, N. Kaiser, W. Weise, Hyperon–nucleon three-body forces and strangeness in neutron stars, Eur. Phys. J. A 56 (2020) 175.
[32] D. Logoteta, I. Vidaña, I. Bombaci, Impact of chiral hyperonic three-body forces on neutron stars, Eur. Phys. J. A 55 (2019) 207.
[33] L. Fabbietti, V. Mantovani Sarti, O. Vazquez Doce, Study of the strong interaction among hadrons with correlations at the LHC, Annu. Rev. Nucl. Part. Sci. 71 (2021) 377–402.
[34] S. Acharya, et al., ALICE, Exploring the NΛ–NΣ coupled system with high precision correlation techniques at the LHC, Phys. Lett. B 833 (2022) 137272.
[35] S. Acharya, et al., ALICE, Investigation of the p–Σ0 interaction via femtoscopy in pp collisions, Phys. Lett. B 805 (2020) 135419.
[36] S. Acharya, et al., ALICE, First observation of an attractive interaction between a proton and a cascade baryon, Phys. Rev. Lett. 123 (2019) 112002.
[37] A. Collaboration, et al., ALICE, Unveiling the strong interaction among hadrons at the LHC, Nature 588 (2020) 232–238, Erratum: Nature 590 (2021) E13.
[38] S. Acharya, et al., ALICE, First measurement of the Λ–Ξ interaction in proton–proton collisions at the LHC, Phys. Lett. B 844 (2023) 137223.
[39] J. Adamczewski-Musch, et al., HADES, The $\boldsymbol{\Lambda p}$ interaction studied via femtoscopy in p + Nb reactions at $\sqrt{s_{\rm NN}} = \mathbf{3.18\ GeV}$, Phys. Rev. C 94 (2016) 025201.
[40] K. Aoki, et al., Extension of the J-PARC hadron experimental facility: third white paper, arXiv:2110.04462, 2021.
[41] Future high-energy pp programme with ALICE, ALICE-PUBLIC-2020-005, CERN-LHCC-2020-018, LHCC-G-179, 2020.
[42] A.R. Bodmer, Q.N. Usmani, J. Carlson, Binding energies of hypernuclei and three-body ΛNN forces, Phys. Rev. C 29 (1984) 684–687.
[43] F.-Q. Wang, S. Pratt, Lambda proton correlations in relativistic heavy ion collisions, Phys. Rev. Lett. 83 (1999) 3138–3141.
[44] S. Acharya, et al., ALICE, Search for a common baryon source in high-multiplicity pp collisions at the LHC, Phys. Lett. B 811 (2020) 135849.
[45] H. Le, J. Haidenbauer, U.-G. Meißner, A. Nogga, Implications of an increased Λ-separation energy of the hypertriton, Phys. Lett. B 801 (2020) 135189.
[46] S. Petschauer, N. Kaiser, Relativistic SU(3) chiral baryon-baryon Lagrangian up to order q^2, Nucl. Phys. A 916 (2013) 1–29.
[47] D.L. Mihaylov, V. Mantovani Sarti, O.W. Arnold, L. Fabbietti, B. Hohlweger, A.M. Mathis, A femtoscopic correlation analysis tool using the Schrödinger equation (CATS), Eur. Phys. J. C 78 (2018) 394.
[48] M.A. Lisa, S. Pratt, R. Soltz, U. Wiedemann, Femtoscopy in relativistic heavy ion collisions, Annu. Rev. Nucl. Part. Sci. 55 (2005) 357–402.
[49] D. Mihaylov, J. González González, Novel model for particle emission in small collision systems, Eur. Phys. J. C 83 (2023) 590.
[50] S. Acharya, et al., ALICE, Common femtoscopic hadron-emission source in pp collisions at the LHC, arXiv:2311.14527, 2023.
[51] A. Collaboration ALICE, Supplemental figures: "Search for a common baryon source in high-multiplicity pp collisions at the LHC", 2023, CERN-EP-2020-053.
[52] R.B. Wiringa, V.G.J. Stoks, R. Schiavilla, An accurate nucleon-nucleon potential with charge independence breaking, Phys. Rev. C 51 (1995) 38–51.
[53] H. Le, J. Haidenbauer, U.-G. Meißner, A. Nogga, Separation energies of light Λ hypernuclei and their theoretical uncertainties, Eur. Phys. J. A 60 (2024) 3.
[54] M. Kohno, H. Kamada, K. Miyagawa, Contributions of 2π-exchange, 1π-exchange, and contact three-body forces in NNLO ChEFT to ${}^3_\Lambda$H, arXiv:2311.10923, 2023.
[55] W.H. Press, S.A. Teukolsky, W.T. Vetterling, B.P. Flannery, Numerical Recipes 3rd Edition: The Art of Scientific Computing, 3 ed., Cambridge University Press, New York, NY, USA, 2007.
[56] S. Petschauer, J. Haidenbauer, N. Kaiser, U.-G. Meißner, W. Weise, Hyperons in nuclear matter from SU(3) chiral effective field theory, Eur. Phys. J. A 52 (2016) 15.
[57] D.R. Entem, R. Machleidt, Accurate charge dependent nucleon nucleon potential at fourth order of chiral perturbation theory, Phys. Rev. C 68 (2003) 041001.
[58] F. Sammarruca, L. Coraggio, J.W. Holt, N. Itaco, R. Machleidt, L.E. Marcucci, Toward order-by-order calculations of the nuclear and neutron matter equations of state in chiral effective field theory, Phys. Rev. C 91 (2015) 054311.
[59] J. Hu, Y. Zhang, E. Epelbaum, U.-G. Meißner, J. Meng, Nuclear matter properties with nucleon-nucleon forces up to fifth order in the chiral expansion, Phys. Rev. C 96 (2017) 034307.
[60] T.A. Rijken, V.G.J. Stoks, Y. Yamamoto, Soft core hyperon - nucleon potentials, Phys. Rev. C 59 (1999) 21–40.
[61] S. Petschauer, J. Haidenbauer, N. Kaiser, U.-G. Meißner, W. Weise, Density-dependent effective baryon–baryon interaction from chiral three-baryon forces, Nucl. Phys. A 957 (2017) 347–378.
[62] A. Kievsky, E. Garrido, M. Viviani, L.E. Marcucci, L. Serksnyte, R. Del Grande, The nnn and ppp correlation functions, arXiv:2310.10428, 2023.
[63] S. Acharya, et al., ALICE, Towards the understanding of the genuine three-body interaction for p–p–p and p–p–Λ, Eur. Phys. J. A 59 (2023) 145.